Hierarchical ZnCo CNFs@CNTs as High-Performance Bifunctional Air Electrodes for Rechargeable Zinc-Air Batteries

Zhixin Wang , Yingjie Chen * , Likai Jin , Fanzhen Kong , Beili Pang , Qian Zhang , Jianguang Feng , Liyan Yu , Lifeng Dong

Posted Date: 9 February 2026

doi: 10.20944/preprints202602.0665.v1

Keywords: hierarchical structure; carbon nanofibers (CNFs); carbon nanotubes (CNTs); bifunctional oxygen electrocatalysis; zinc-air batteries (ZABs)

 doi:10.20944/preprints202602.0665.v1

Article

Hierarchical ZnCo CNFs@CNTs as High-Performance Bifunctional Air Electrodes for Rechargeable Zinc-Air Batteries

Zhixin Wang [1], Yingjie Chen [1,*], Likai Jin [1], Fanzhen Kong [1], Beili Pang [1], Qian Zhang [1], Jianguang Feng [1], Liyan Yu [1]and Lifeng Dong [1,2,*]

[1] College of Materials Science and Engineering, Qingdao University of Science and Technology, Qingdao 266042, P. R. China

[2] Department of Physics, Hamline University, St. Paul 55104, USA

* Correspondence: chenyingjie@qust.edu.cn (Y.J.C.); ldong03@hamline.edu (L.D.)

Abstract

Carbon-based bifunctional oxygen electrocatalysts with rationally designed architectures are essential for high-performance rechargeable zinc-air batteries (ZABs), yet the concurrent optimization of catalytic activity, durability, and mass transport remains challenging. Herein, hierarchical ZnCo carbon nanofibers/carbon nanotubes (CNFs@CNTs) are fabricated via single-nozzle electrospinning followed by melamine-assisted pyrolysis under a $ZnCl_2$-regulated atmosphere. During thermal treatment, Co species embedded within carbon nanofibers catalyze in situ carbon nanotube growth, while $ZnCl_2$ vapor modulates the carbonization process and surface chemistry, collectively generating a hierarchical CNFs@CNTs architecture with high surface area and abundant exposed active sites. As a result, ZnCo CNFs@CNTs exhibit outstanding bifunctional ORR/OER activity, surpassing Zn-free and Co-free counterparts. Combined structural and electrochemical analyses reveal that the synergistic interaction between Co active centers and Zn-assisted carbon structural regulation enhances reaction kinetics and long-term stability. When implemented as air electrodes in rechargeable ZABs, ZnCo CNFs@CNTs deliver high power density, reduced charge-discharge polarization, and excellent cycling durability, demonstrating strong practical applicability. This work presents an effective strategy for constructing hierarchical CNFs@CNTs composites via electrospinning and dual-component thermal regulation, offering new insights into the design of high-efficiency bifunctional air electrodes for advanced ZABs.

Keywords: hierarchical structure; carbon nanofibers (CNFs); carbon nanotubes (CNTs); bifunctional oxygen electrocatalysis; zinc-air batteries (ZABs)

1. Introduction

In rechargeable zinc-air batteries, air electrodes must simultaneously drive the oxygen reduction reaction (ORR) during discharge and the oxygen evolution reaction (OER) during charge [1–3]. The sluggish kinetics and distinct reaction pathways impose stringent and synergistic requirements on the configuration of catalytic active sites, interfacial stability, and mass transport properties. Although noble-metal-based catalysts exhibit high activity for individual reactions, their high cost and limited durability in alkaline media hinder practical applications[4–7]. Therefore, developing efficient, stable, and scalable non-precious bifunctional oxygen electrocatalysts remains a critical challenge[8–12].

Carbon-based composite materials have attracted considerable attention as oxygen electrocatalysts due to their excellent electrical conductivity and tunable structures[13,14]. Modulating the local chemical environment of carbon supports can significantly influence the distribution of metal active sites and reaction pathways. For instance, controlling surface features in

 doi:10.20944/preprints202602.0665.v1

bamboo-like carbon nanotubes enables uniform noble-metal deposition, thereby improving catalytic utilization efficiency [15]. Similarly, integrating transition-metal species with carbon matrices can enhance the adsorption and conversion of oxygen intermediates at the reaction interface[16]. These studies highlight that carbon supports not only provide structural scaffolds but also actively regulate electrocatalytic performance through their microchemical environment.

Among carbon-based architectures, carbon nanofibers (CNFs) are attractive scaffolds for self-supporting air electrodes owing to their continuous one-dimensional structure and mechanical robustness. Incorporating carbon nanotubes (CNTs) onto CNF backbones further establishes hierarchical conductive networks, shortening electron and reactant transport pathways. Biomimetic designs that enrich N-doped CNTs within CNFs have been shown to simultaneously enhance ORR and OER activity[17–20], while synergistic interactions among multiple active components in CNF/CNT composites improves both power density and cycling stability in Zn-air batteries [21].

From the perspective of active species, cobalt exhibits high OER activity in alkaline media and can catalyze carbon structural reconstruction at elevated temperatures. Encapsulating cobalt nanoparticles within N-doped CNFs or CNTs suppresses metal aggregation and enhances reaction stability [6]. Further interface engineering or coordination modulation strategies can introduce diverse active sites, such as Co-N-C motifs, metal-carbon heterojunctions, or alloy structures, thereby strengthening bifunctional catalytic performance[22,23]. However, single-metal systems often exhibit unbalanced ORR and OER activity, limiting their overall performance in rechargeable systems.

Multimetallic strategies have therefore attracted increasing interest. Introducing a secondary metal or constructing bimetallic heterostructures can tune electronic structures and optimize the adsorption energies of oxygen intermediates [24,25]. In zinc-air battery systems, Zn incorporation not only modulates electronic properties but can also induce porosity evolution or form unique coordination environments during thermal treatment, thereby enhancing overall electrochemical performance[26]. Moreover, gas-phase or in situ reconstruction strategies have proven effective in stabilizing bimetallic interfaces and carbon-encapsulated structures, preserving active-site integrity during extended cycling[27,28].

Electrospinning provides a versatile route for integrating multiple components and building hierarchical architectures. By tailoring precursor composition and post-treatment conditions, controlled metal dispersion, heteroatom doping, and porous structures can be achieved within individual fibers[27]. Coupling high-temperature gas-phase modulation or impregnation strategies enables simultaneous carbonization, N-doping, and metal structural reconstruction, yielding well-defined CNF/CNT hybrid structures. Despite advances in interface engineering and heterostructure design[29,30], a systematic understanding of in situ CNT growth, bimetallic synergy, and their influence on ORR/OER active site evolution remains limited.

Motivated by these considerations, this work employs single-nozzle electrospinning to fabricate cobalt-containing polymer nanofiber precursors, achieving uniform Co dispersion within PAN-derived carbon fibers. Subsequent melamine-assisted pyrolysis under a $ZnCl_2$-regulated atmosphere induces carbonization, N-doping, and in situ CNT growth on the CNF surface, constructing hierarchical CNFs@CNTs composites. By comparing samples prepared with and without $ZnCl_2$ and varying metal compositions, we systematically investigate their effects on microstructural evolution and bifunctional oxygen electrocatalytic performance. Finally, the optimized materials are assembled into zinc-air batteries to evaluate their practical performance in energy conversion devices.

 doi:10.20944/preprints202602.0665.v1

2. Results and Discussion

2.1. Structural Characterizations and Composition Analysis

The synthesis process of ZnCo CNFs@CNTs is illustrated in Scheme 1. $Co(CH_3COO)_2{\cdot}4H_2O$ was first uniformly incorporated into a PAN solution, and one-dimensional Co NFs precursor nanofibers were prepared via uniaxial electrospinning, ensuring homogeneous dispersion of Co species within the fiber skeleton. The Co NFs precursor was then subjected to heat treatment in a double-boat tube furnace, where melamine ($C_3H_6N_6$) was placed downstream of the Co NFs as a carbon/nitrogen source, while $ZnCl_2$ in the upstream boat created a regulated gas-phase environment. During pyrolysis, melamine decomposed to release active C and N species, inducing in-situ CNT growth on the fiber surface under Co catalysis. Meanwhile, $ZnCl_2$ sublimation enabled Zn species to migrate downstream, participating in structural evolution and modulating the carbon surface chemistry. As a result, a hierarchical CNFs@CNTs composite consisting of continuous and flexible carbon nanofibers decorated with CNTs was obtained, providing enhanced specific surface area and active site exposure. The final product was denoted as ZnCo CNFs@CNTs.

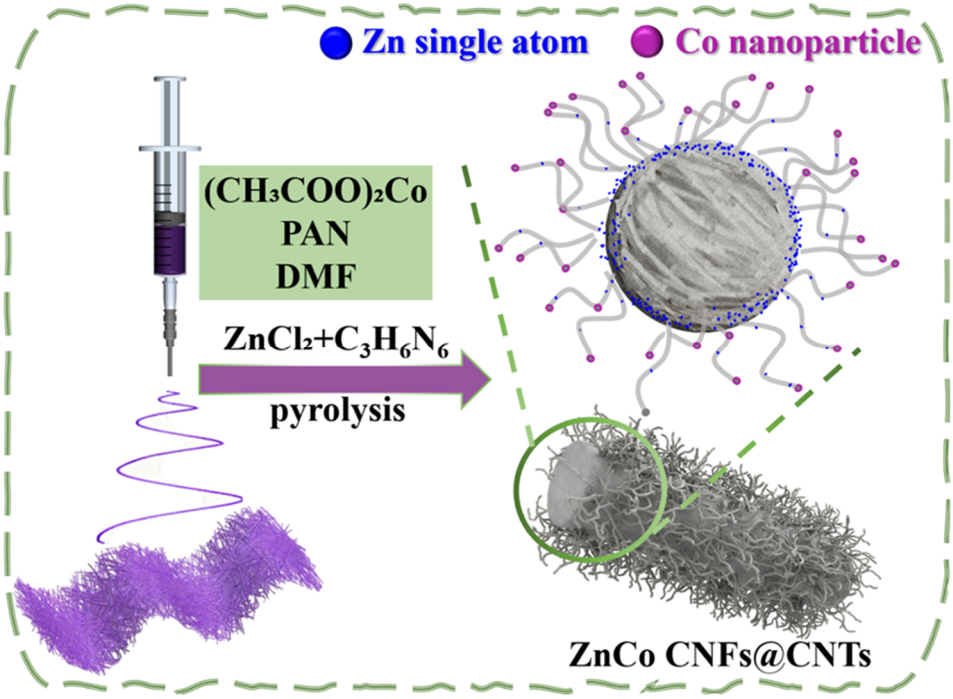

Scheme 1. Schematic illustration depicting the synthesis process of ZnCo CNFs@CNTs.

The morphological structure and elemental distribution of Zn CNFs were systematically characterized (Figure S1). SEM images (Figure S1a) reveal that Zn CNFs retain a continuous one-dimensional nanofiber network with smooth surfaces, indicating that the fiber morphology is well maintained after $ZnCl_2$ introduction and high-temperature carbonization. AC HAADF-STEM and elemental mapping analyses (Figure S1b-c) show that Zn species are uniformly dispersed as single atoms within the N-doped carbon skeleton, while C, N, and Cl are also homogeneously distributed, confirming effective nitrogen doping and atomic-level Zn dispersion.

ZnCo CNFs@CNTs display a hierarchical structure, in which CNTs grow in situ on carbon nanofibers to form a three-dimensional conductive network, as confirmed by SEM and TEM images (Figures 1a-b). A tightly bonded interface between CNTs and CNFs is observed, and Co nanocrystals with a lattice spacing of ~0.20 nm, corresponding to the Co (111) plane, act as catalytic centers for CNT growth (Figure 1c). EDS elemental mapping (Figure 1d) confirms the uniform distribution of Zn, Co, N, O, and Cl, with Zn and Cl mainly present as highly dispersed atoms or ultrafine clusters. These structural characteristics provide abundant active sites, high surface area, and efficient electron

 doi:10.20944/preprints202602.0665.v1

and mass transport pathways, establishing a robust framework for bifunctional oxygen electrocatalysis.

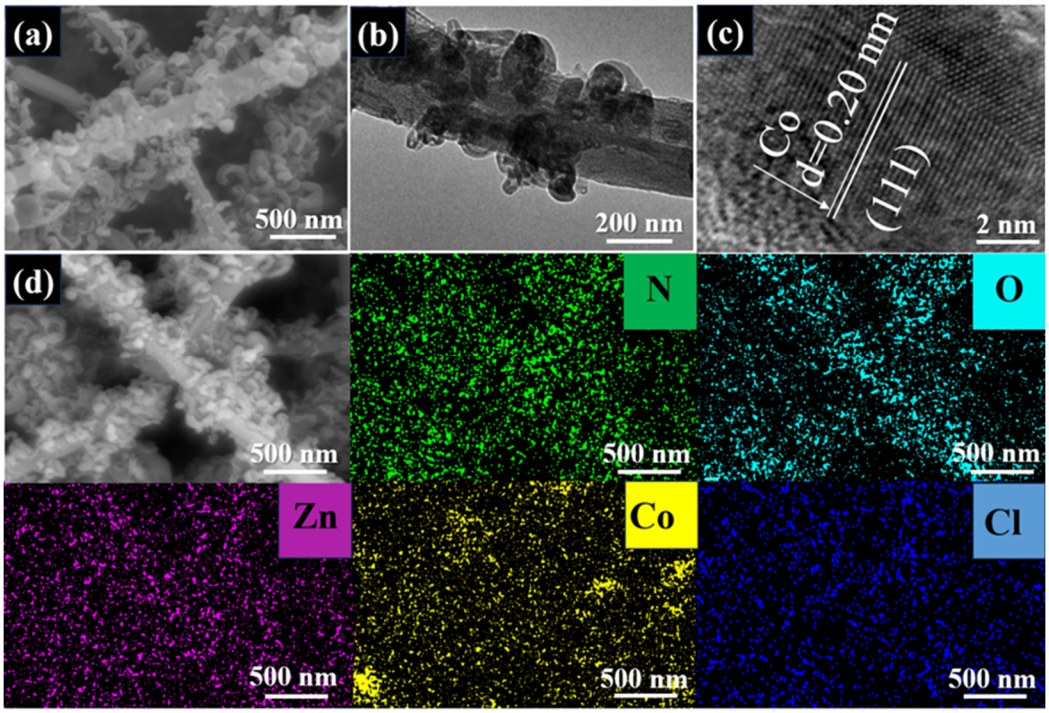

Figure 1. Morphology and elemental distribution characterization of ZnCo CNFs@CNTs. (a) SEM image; (b) TEM image; (c) HRTEM image; (d) SEM image with corresponding EDS elemental mapping (Zn, Co, N, O, and Cl).

Figure 2 compares the structural characteristics of different samples. N_2 adsorption-desorption isotherms (Figure 2a) indicate that ZnCo CNFs@CNTs, Co CNFs@CNTs, and Zn CNFs exhibit typical type IV behavior with hysteresis loops, indicating dominant mesoporous structures. Notably, ZnCo CNFs@CNTs display higher adsorption at low relative pressure (P/P_0<0.1), suggesting additional microporosity and a higher specific surface area, which favors active-site exposure. Pore size distribution curves (Figure 2b) reveal that ZnCo CNFs@CNTs possess a concentrated mesoporous range of 5-15 nm while retaining larger pores, forming a hierarchical micro-mesoporous structure that facilitates mass transport and gas diffusion.

 doi:10.20944/preprints202602.0665.v1

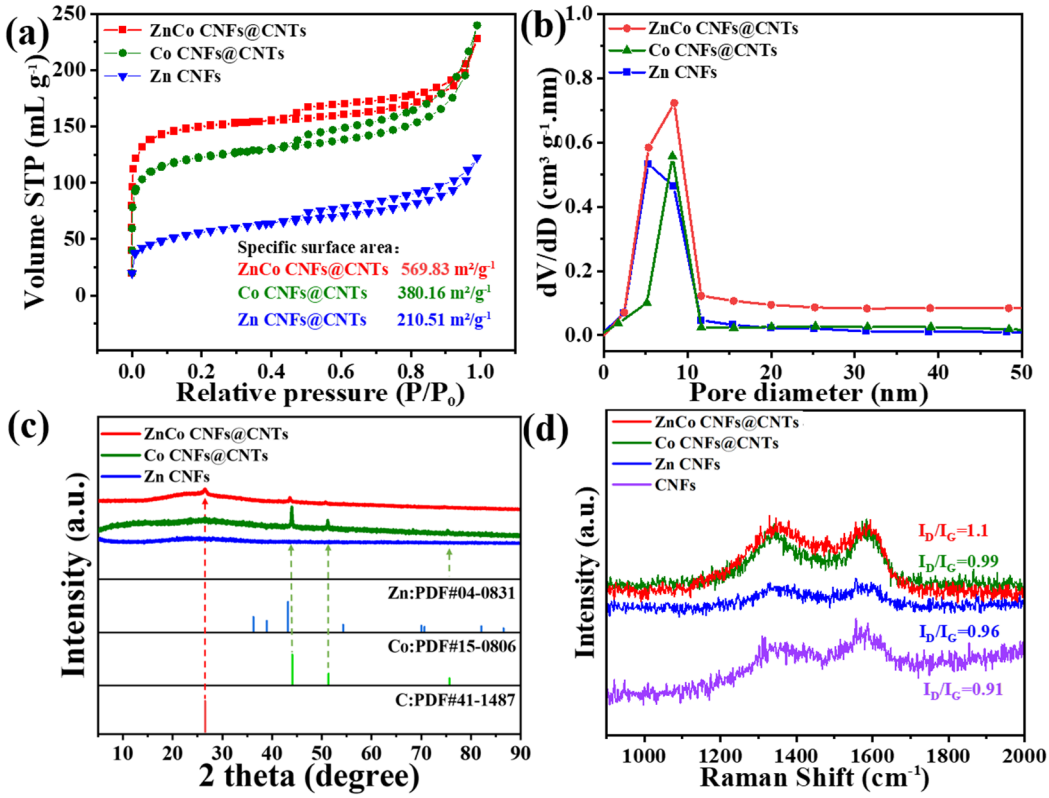

Figure 2. (a) N_2 adsorption-desorption isotherms; (b) pore size distribution curves; and (c) XRD patterns of of ZnCo CNFs@CNTs, Co CNFs@CNTs, and Zn CNFs; (d) Raman spectra of ZnCo CNFs@CNTs, Co CNFs@CNTs, Zn CNFs and CNFs.

XRD patterns (Figure 2c) show a broad diffraction peak at ~26° for all samples, corresponding to the (002) plane of graphitized carbon, indicative of low crystallinity. Weak metallic Co peaks are observed for Co CNFs@CNTs and ZnCo CNFs@CNTs, confirming partial reduction to small Co nanocrystals. In contrast, Zn CNFs show no discernible Zn or ZnO peaks, consistent with highly dispersed or amorphous Zn species. Raman spectra (Figure 2d) display characteristic D and G bands at ~1350 and 1580 cm^{-1}, respectively. The highest I_D/I_G ratio is observed for ZnCo CNFs@CNTs, reflecting an increased defect density induced by Zn/Co synergistic effects and in-situ CNT growth, which enhances active site anchoring and electronic structure modulation.

Overall, ZnCo CNFs@CNTs integrate hierarchical porosity, high surface area, Co nanocrystals, and enriched carbon defects, providing a favorable structural foundation for superior electrocatalytic performance.

Figure 3 presents the surface elemental composition and chemical states of ZnCo CNFs@CNTs. The survey XPS spectrum (Figure 3a) shows the presence of C, N, O, Zn, Co, and Cl, confirming successful multiple element incorporation into the N-doped carbon framework. High-resolution C 1s spectra (Figure 3b) reveal C-C/C=C, C-N/C-Cl, and O-C=O/C=O bonds, reflecting a rich heteroatom environment capable of modulating the local electronic structure. The N 1s spectrum (Figure 3c) can be deconvoluted into pyridinic, pyrrolic, graphitic, and oxidized nitrogen species. Pyridinic and graphitic nitrogen act as active sites for ORR and OER, while pyrrolic nitrogen increases defect density and stabilizes metal species. The O 1s spectra (Figure 3d) show C-O, C=O, and O-C=O/C=O-C-N groups, which can enhance metal-support interactions and structural stability. Zn 2p spectra (Figure 3e) indicate that Zn exists predominantly in ionic or coordinated states rather than metallic Zn, promoting dispersion and electronic regulation. Co 2p spectra (Figure 3f) show oxidized Co species forming Co-N_x/Co-O_x structures, which serve as key active centers for bifunctional oxygen catalysis. Cl 2p spectra (Figure 3g) reveal the presence of organic Cl and Zn-Cl species, further modulating the electronic environment of Zn sites and influencing intermediate adsorption.

 doi:10.20944/preprints202602.0665.v1

Collectively, XPS results confirms the synergistic incorporation of Zn, Co, N, and Cl into the carbon framework, generating a complex chemical environment that underpins the excellent ORR/OER performance of ZnCo CNFs@CNTs.

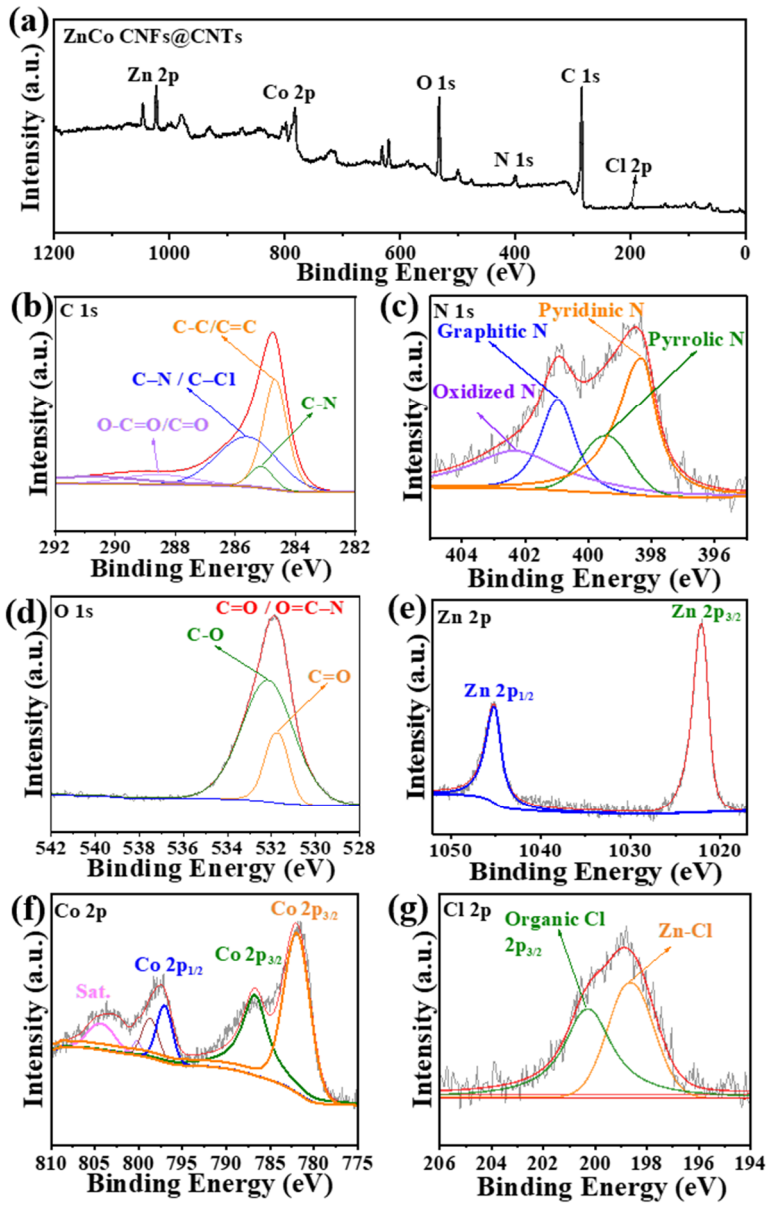

Figure 3. XPS spectra of ZnCo CNFs@CNTs: (a) survey spectrum, (b) C 1s, (c) N 1s, (d) O 1s, (e) Zn 2p, (f) Co 2p and (g) Cl 2p.

2.2. Electrocatalytic Properties

Figure 4 compares the electrocatalytic performance of five different catalysts toward the oxygen reduction reaction (ORR) and oxygen evolution reaction (OER). At a scanning rate of 10 mV·s^{-1}, the ORR polarization curves (Figure 4 a) show that ZnCo CNFs@CNTs exhibit the highest catalytic activity, delivering a half-wave potential of 0.86 V. This value is significantly higher than that of the commercial Pt/C catalyst (0.83 V) and other comparative samples (Co CNFs@CNTs: 0.81 V; Zn CNFs: 0.80 V; CNFs: 0.76 V), and surpasses many previously reported ORR catalysts (Table S1)[31–35]. The corresponding Tafel plot (Figure 4b) indicates that ZnCo CNFs@CNTs possess the lowest Tafel slope (74.7 mV·dec^{-1}), reflecting more favorable ORR kinetics. For OER, ZnCo CNFs@CNTs also show outstanding performance, requiring an overpotential of only 1.64 V, which is lower than that of commercial RuO_2 (1.75 V) and other comparative catalysts (Figure 4c). The OER Tafel slope (Figure

 doi:10.20944/preprints202602.0665.v1

4d) of 92.6 mV·dec^{-1} further confirms faster charge-transfer kinetics and a reduced reaction energy barrier. Overall, ZnCo CNFs@CNTs demonstrate excellent bifunctional catalytic activity for both ORR and OER, which can be attributed to the synergistic interaction between Zn and Co species and the highly conductive CNT network. These features promote efficient electron transfer and optimized adsorption/desorption of reaction intermediates, thereby markedly enhancing catalytic efficiency and highlighting the potential of ZnCo CNFs@CNTs for zinc-air battery applications.

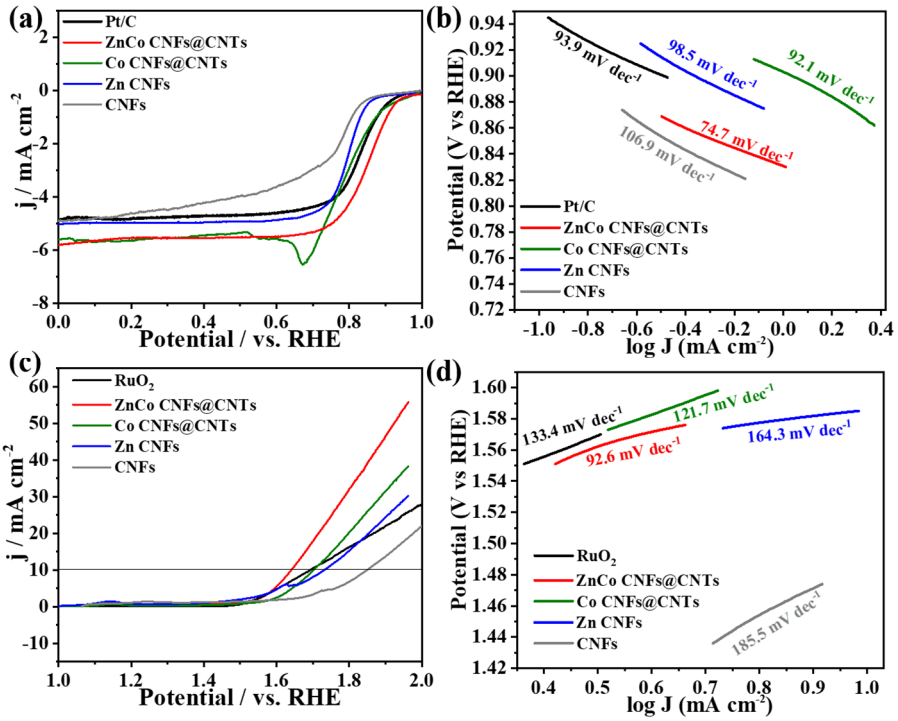

Figure 4. (a) ORR performance curves of five catalysts at 10 mV s^{-1} at 1600 rpm and (b) corresponding Tafel plots; (c) OER performance curves of five catalysts at 10 mV s^{-1} at 1600 rpm and (d) corresponding Tafel plots.

A comprehensive analysis of Figure 5 further demonstrates that ZnCo CNFs@CNTs exhibit excellent ORR activity with a well-defined four-electron reaction pathway. The linear sweep voltammograms recorded at different rotation speeds (400-2500 rpm, Figure 5a) show a pronounced increase in limiting diffusion current density with increasing rotation speed, while the half-wave potential remains nearly unchanged, indicating favorable mass transfer behavior and kinetic stability. The corresponding Koutecky-Levich plots shown as the inset of Figure 5a yield an electron transfer number of 3.81, close to the ideal four-electron pathway. Electrochemical impedance spectroscopy (EIS) (Figure 5b) reveals that ZnCo CNFs@CNTs has the lowest charge-transfer resistance (Rct), suggesting fast interfacial charge transport and favorable ORR/OER kinetics. Rotating ring-disk electrode (RRDE) measurements (Figure 5c) further confirm a half-wave potential of 0.86 V, exceeding that of Pt/C (0.83 V), while maintaining a comparable limiting current density, indicative of superior intrinsic activity. Moreover, the hydrogen peroxide yield remains below 10% over the entire potential range (Figure 5d), significantly lower than that of Pt/C (>10%), with an electron transfer number consistently between 3.8 and 3.9. These results confirm that ZnCo CNFs@CNTs predominantly catalyze ORR via a highly selective four-electron pathway. The enhanced ORR performance arises from the synergistic Zn–Co bimetallic sites and the interconnected carbon fiber/CNT network, which together optimize the adsorption and desorption energetics of oxygen intermediates.The durability of ZnCo CNFs@CNTs toward ORR and OER was evaluated by chronoamperometric measurements (Figure S2). After 30,000 s of continuous operation, ZnCo CNFs@CNTs retain 92.58% of their initial ORR current, which is substantially higher than that of Pt/C (80.13%, Figure S2a). For OER at 1.65 V vs. RHE, ZnCo CNFs@CNTs maintain 83.57% of the initial

 doi:10.20944/preprints202602.0665.v1

current, outperforming RuO_2, which retains only 68.26% (Figure S2b). This excellent durability is attributed to the hierarchical CNFs@CNTs architecture, in which electrospun CNFs provide a robust conductive backbone, in-situ grown CNTs enhance rapid electron transport, and synergistically anchored Zn and Co sites stabilize the active centers. As a result, catalyst degradation and active-site deactivation are effectively suppressed, enabling long-term bifunctional electrocatalytic stability superior to that of precious-metal-based catalysts.

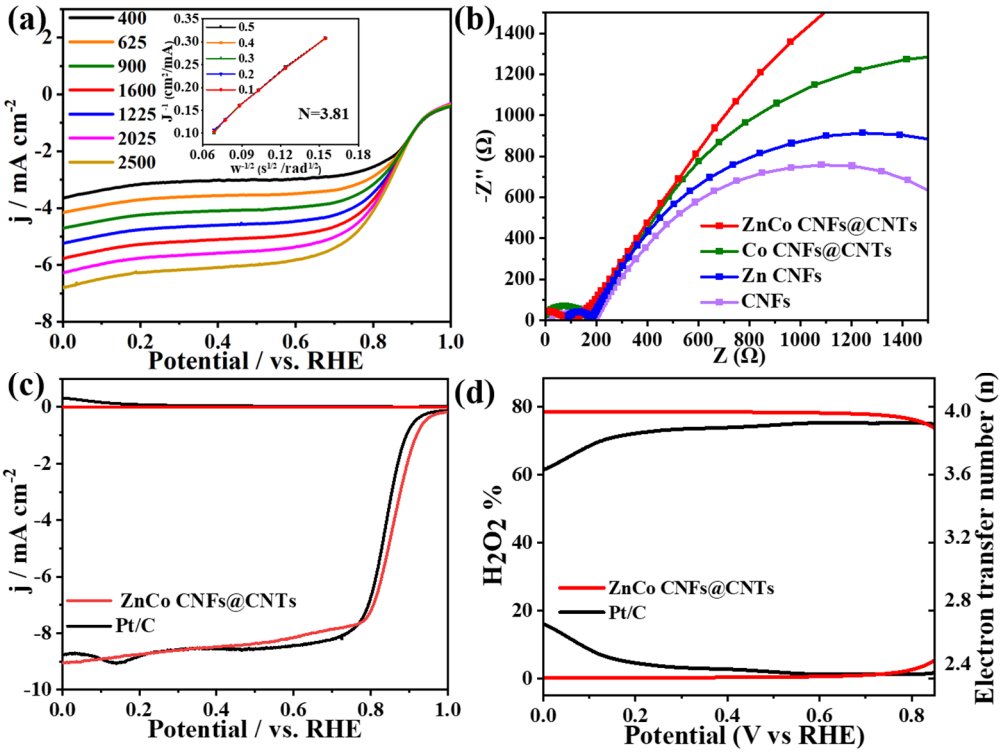

Figure 5. (a) LSV curves at different rotation speeds, with the corresponding K-L plots of ZnCo CNFs@CNTs; (b) Comparative Nyquist plots for the four samples; (c) RRDE measurements and (d) H_2O_2 yield and electron transfer number of ZnCo CNFs@CNTs and Pt/C.

2.3. Aqueous Zn-Air Battery Performance

To evaluate the practical application potential of ZnCo CNFs@CNTs, liquid and self-supporting flexible Zn-air batteries (ZABs) were assembled and systematically compared with Pt/C + RuO_2 benchmark systems. As shown in Figure 6a, ZnCo CNFs@CNTs were employed as the air cathode. The resulting battery exhibits an open-circuit voltage (OCV) of 1.44 V, higher than that of the noble-metal benchmark. Furthermore, a maximum power density of 132.1 mW cm^{-2} is achieved, significantly higher than the 100.7 mW cm^{-2} obtained for the Pt/C+RuO_2 reference battery (Figures 6b-d). The ZnCo CNFs@CNTs-based battery also delivers a higher specific capacity of 808.5 mAh g^{-1}, compared with 694.7 mAh g^{-1} for the control system, while the charge-discharge voltage gap is reduced to 1.25 V, indicating improved reversibility and energy efficiency. Notably, stable operation is maintained for 1316 h at a current density of 5 mA cm^{-2}, demonstrating excellent cycle durability (Figure 6e). Theses results confirm the strong application potential and scalability of ZnCo CNFs@CNTs as efficient bifunctional air cathodes for ZABs.

 doi:10.20944/preprints202602.0665.v1

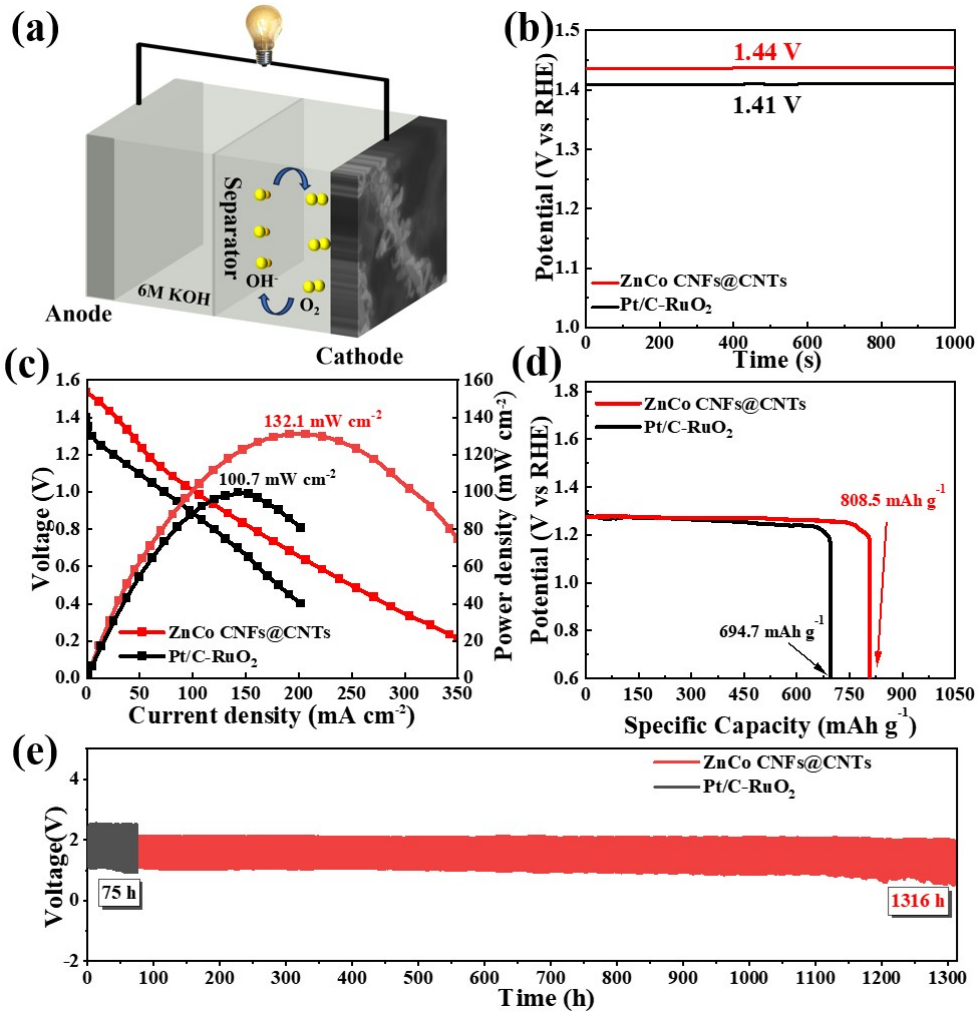

Figure 6. (a) Schematic illustration of ZABs ; (b) OCV comparison; (c) discharge polarization and corresponding power density curves; (d) specific discharge capacity; and (e) galvanostatic cycling stability at 5 mA cm^{-2} for ZnCo CNFs@CNTs and Pt/C–RuO_2 air electrodes.

2.4. Solid-State Zn-Air Battery Performance

Figure 7a illustrates the configuration of a flexible, self-supporting solid-state ZAB assembled using a ZnCo CNFs@CNTs air cathode. The battery delivers an open-circuit voltage of 1.40 V (Figure 7b), indicating good thermodynamic stability. During charge - discharge cycling, a low polarization voltage is maintained, and a peak power density of 123.2 mW·cm^{-2} is achieved (Figure 7c), reflecting rapid reaction kinetics. Practical demonstration shows that a single flexible battery can stably power a red light-emitting diode (LED) (Figure 7d). After 110-h of constant-current cycling, the battery remains stable within a voltage window of 1.13 V without noticeable degradation (Figure 7e), confirming its electrochemical durability and mechanical integrity. In addition, Figure S3a and b display the morphology of ZnCo CNFs@CNTs under bending and folding conditions, where the structure remains intact without fracture, indicating excellent flexibility and mechanical robustness. These characteristics meet the mechanical requirements of wearable energy-storage devices. Overall, ZnCo CNFs@CNTs combine high bifunctional catalytic activity with structural flexibility, demonstrating strong potential for next-generation wearable zinc-air batteries.

 doi:10.20944/preprints202602.0665.v1

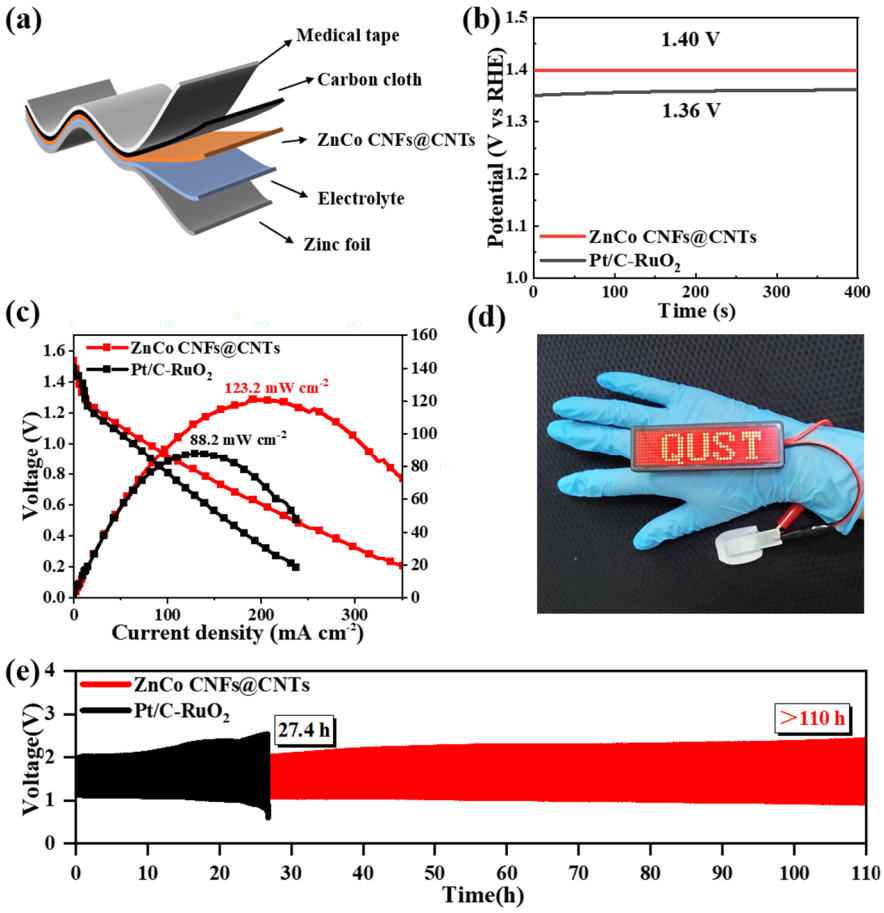

Figure 7. (a) Schematic illustration of flexible self-supporting ZABs, (b) open-circuit voltage, (c) discharge polarization and power density curves compared with Pt/C–RuO_2, (d) photograph of a red LED powered by a flexible ZnCo CNFs@CNTs battery, and (e) charge–discharge cycling performance.

3. Experimental

3.1. Materials

Polyacrylonitrile (PAN, Mw = 150,000) was purchased from Macklin. N,N-Dimethylformamide (DMF, ≥99.5%), melamine ($C_3H_6N_6$, ≥98%), zinc chloride ($ZnCl_2$, ≥98%), and cobalt(II) acetate tetrahydrate ($Co(CH_3COO)_2{\cdot}4H_2O$, AR) were supplied by Aladdin Industrial Corporation. Isopropanol (≥99.9%) and Nafion 117 (5 wt.%) were purchased from Sigma.

3.2. Synthesis of Nanofiber Precursors NFs and Co NFs

Nanofiber precursors were prepared by uniaxial electrospinning. Taking Co NFs as a representative example, 5.13 mmol of polyacrylonitrile (PAN) was dissolved in 7 mL of N,N-dimethylformamide (DMF) and magnetically stirred at 50 °C for 1 h to obtain a homogeneous polymer solution. Subsequently, 5.52 mmol of cobalt acetate ($Co(CH_3COO)_2{\cdot}4H_2O$) was added, and the mixture was stirred for an additional 10 h to form a uniform spinning precursor solution. Electrospinning was conducted at an applied voltage of 18 kV, a tip-to-collector distance of 16 cm, and a solution feeding rate of 0.6 mL h^{-1}, with an ambient temperature of 25-30 °C, relative humidity of 30-40%, and a collector rotation speed of 120 rpm. The as-spun nanofiber membrane was dried overnight at 60 °C and denoted as Co NFs. Under the same conditions, nanofibers prepared without introducing metal salts were denoted as NFs.

 doi:10.20944/preprints202602.0665.v1

3.3. Synthesis of CNFs, Zn CNFs, Co CNFs@CNTs and ZnCo CNFs@CNTs

The nanofiber precursors were placed in a porcelain boat, and 7.93 mmol of melamine was evenly distributed above the fiber samples as a nitrogen source. For Zn-containing samples, an additional porcelain boat containing 11 mmol of $ZnCl_2$ was placed upstream as the zinc source. The boats were then placed sequentially in a tube furnace for heat treatment. The samples were first heated to 280 °C at a heating rate of 3 °C min^{-1} in air and held for 1 h to stabilize the precursors. Subsequently, under an N_2 atmosphere, the temperature was increased to 900 °C at 5 °C min^{-1} and maintained for 2 h to complete carbonization and nitrogen-doping. The obtained samples were designed as follows: CNFs, obtained from NFs via carbonization with melamine burial; Co CNFs@CNTs, obtained from Co NFs under identical conditions; Zn CNFs, prepared by introducing $ZnCl_2$ during the carbonization and nitrogen-doping processes of NFs; and ZnCo CNFs@CNTs prepared by simultaneously introducing $ZnCl_2$ during the carbonization and nitrogen-doping processes of Co NFs with melamine burial.

3.4. Electrochemical Measurements

Electrochemical performances were assessed using a standard three-electrode system with a CHI 760E workstation. Measurements were performed in saturated N_2 or O_2 in 0.1 M KOH, with an Ag/AgCl reference electrode and a graphite rod counter electrode. Working electrodes were prepared by mixing 4 mg of sample, 1 mg carbon black (XC-72), 800 μL deionized water, 200 μL isopropanol, and 20 μL Nafion117 , followed by 20 min sonication. The resulting suspension was applied to glassy-carbon electrodes of rotating disk electrodes (RDE, 3 mm diameter) or rotating ring-disk electrodes (RRDE, 4 mm diameter) to achieve a loading of 60 μg cm^{-2} and air-dried.

ORR polarization curves were obtained using rotating disk experiments (RDE-3A, ALS Co.) from 0.2 V to -0.8 V (vs. Ag/AgCl) at 10 mV s^{-1} with rotation speeds of 400-2500 rpm in O_2-saturated 0.1 M KOH. OER performance was evaluated using linear sweep voltammetry (LSV) at 10 mV s^{-1} in O_2-saturated 0.1 M KOH. Electrochemical impedance spectroscopy (EIS) was performed at 1.545 V (vs. RHE) over 100 kHz-10 mHz with 10 mV amplitude. Stability tests for ORR and OER were conducted by chronoamperometry in a three-electrode system under stirring at a constant potential.

Reference potentials were converted to the reversible hydrogen electrode (RHE) using the Nernst equation:

$$E_{RHE} = E_{Ag/AgCl} + 0.0591pH + 0.197 \quad (1)$$

where E_{RHE} is the converted potential relative to RHE, and $E_{Ag/AgCl}$ is the real-time value measured by the Ag/AgCl reference electrode.

Cyclic voltammetry (CV) was used to record ORR curves in KOH solution saturated with N_2 or O_2. LSV curves were obtained under similar conditions at a scan rate of 5 mV s^{-1} and various rotational speeds (400, 625, 900, 1225 and 1600 rpm). The electron transfer number (n) was calculated using the Koutecky-Levich (K-L) equation:

$$\frac{1}{J}=\frac{1}{J_k}+\frac{1}{J_d}=\frac{1}{J_k}+\frac{1}{(B\omega^{1/2})} \quad (2)$$

$$B=0.62nFC_0(D_0)^{2/3}\nu^{-1/6} \quad (3)$$

where J is the measured current density, J_k is the kinetic current density, J_d is the diffusion-limited current density, F is the Faraday constant (96,485 C mol^{-1}), D_0 (1.86×10^{-5} cm^2 s^{-1}) and C_0 (1.21×10^{-6} mol cm^{-3}) are the diffusion coefficient and bulk concentration of O_2 in 0.1 M KOH, respectively, ω (rpm) is the rotation rate of RDE, and ν is the kinetic viscosity (0.01 cm^2 s^{-1}).

The electron transfer number (n) and hydrogen peroxide yield (HO_2^-%) in the ORR process were determined using RRDE.

$$n=4\times\frac{I_d}{I_d+I_r/N} \quad (4)$$

 doi:10.20944/preprints202602.0665.v1

$$HO_2^-\%=200\times\frac{I_r/N}{I_d+\frac{I_r}{N}} \quad (5)$$

where I_d is the disk current, I_r is the ring current density, and N is the current collection efficiency constant (0.37).

OER measurements were conducted in 0.1 M KOH solution under O_2 saturation, with a rotation rate of 1600 rpm and a scan rate of 5 mV s^{-1}. The ohmic drop loss was corrected (iR-correct). OER stability was assessed by chronoamperometry at 1.60 V (vs. RHE).

4. Conclusions

Hierarchical ZnCo CNFs@CNTs with dual-metal active centers were successfully fabricated via electrospinning coupled with gas-phase-assisted pyrolysis. The resulting material features carbon nanofibers as a robust scaffold decorated with in situ-grown carbon nanotubes, enabling atomic-level dispersion of Zn species and their synergistic interaction with Co nanocrystals, thereby markedly enhancing bifunctional ORR/OER activity. Electrochemical measurements demonstrate that ZnCo CNFs@CNTs achieve an ORR half-wave potential of 0.86 V and an OER overpotential of 1.64 V, surpassing the performance of commercial Pt/C and RuO_2 catalysts. In liquid Zn-air batteries, the assembled electrodes deliver a high open-circuit voltage of 1.44 V, a peak power density of 132.1 $mW{\cdot}cm^{-2}$, and long-term cycling stability exceeding 1300 h. Furthermore, flexible solid-state batteries achieve an open-circuit voltage of 1.40 V and a peak power density of 123.2 $mW{\cdot}cm^{-2}$, while maintaining stable operation under bending and folding, indicative of excellent mechanical robustness and practical device performance. Collectively, the superior bifunctional catalytic activity, hierarchical architecture, and conductive CNT network facilitate efficient electron/ion transport and optimized intermediate adsorption/desorption, highlighting ZnCo CNFs@CNTs as promising candidates for next-generation wearable energy devices.

Supplementary Materials: The following supporting information can be downloaded at: https://doi.org/10.5281/zenodo.18481234, Figure S1: SEM image of Zn CNFs and AC HAADF-STEM images with corresponding elemental mapping results; Figure S2: Chronoamperometric ORR curves at 0.76 V for ZnCo CNFs@CNTs and Pt/C; and OER stability curves at 1.65 V for ZnCo CNFs@CNTs and RuO_2; Figure S3: Flexibility test of ZnCo CNFs@CNTs; Table S1: Comparison of ORR and OER activities of ZnCo CNFs@CNTs with other recently reported noble metal-free catalysts.

Author Contributions: Zhixin Wang: Conceptualization, Investigation, Software, Writing-original draft. Yingjie Chen: Conceptualization, Methodology, Writing-review & editing. Likai Jin: Investigation. Fanzhen Kong: Conceptualization. Beili Pang: Investigation, Conceptualization. Qian Zhang: Visualization. Jianguang Feng: Investigation, Conceptualization. Liyan Yu: Project administration, Funding acquisition. Lifeng Dong: Project administration, Funding acquisition, Supervision, Writing-review & editing, Resources.

Funding: This work was supported by the National Natural Science Foundation of China (21776147, 21905153, 61604086, 22378221, 22308183, 52002198), the Natural Science Foundation of Shandong Province (ZR2021YQ32, ZR2022QB164,ZR2023QB070), the Taishan Scholar Project of Shandong Province (tsqn201909117), the Qingdao Science and Technology Benefit the People Demonstration and Guidance Special Project (23-2-8-cspz-11-nsh), the Qingdao Natural Science Foundation (23-2-1-241-zyyd-jch), and the China Postdoctoral Science Foundation (2023M731856). L. F. Dong also thanks financial support from the Malmstrom Endowed Fund at Hamline University.

Data Availability Statement: The authors can confirm that all relevant data are included in the article.

Conflicts of Interest: The authors do not have any financial or non-financial interests that are directly or indirectly related to the work submitted for publication.

 doi:10.20944/preprints202602.0665.v1

References

1. Xia, Q.; Zhai, Y.J.; Zhao, L.L.; Wang, J.; Li, D.Y.; Zhang, L.L.; Zhang, J.T. Carbon-supported single-atom catalysts for advanced rechargeable metal-air batteries. *Energy Mater*. **2022**, *2*, 200015.
2. Pan, L.; Chen, D.F.; Pei, P.C.; Huang, S.W.; Ren, P.; Song, X. A novel structural design of air cathodes expanding three-phase reaction interfaces for zinc-air batteries. *Appl. Energy*. **2021**, *290*, 116777.
3. Yin, Z.Y.; He, R.; Xue, H.B.; Chen, J.J.; Wang, Y.; Ye, X.X.; Xu, N.N.; Qiao, J.L.; Huang, H.T. A bimetallic-activated MnO_2 self-assembly electrode with a dual heterojunction structure for high-performance rechargeable zinc-air batteries. *Energy Mater*. **2022**, *2*, 200021.
4. Shi, Q.; Liu, Q.; Ma, Y.; Fang, Z.; Liang, Z.; Shao, G.; Tang, B.; Yang, W.Y.; Qin, L.; Fang, X.S. High-performance trifunctional electrocatalysts based on FeCo/Co_2Phybrid nanoparticles for zinc-air battery and self-powered overall water splitting. *Adv. Energy Mater.* **2020**, *10*, 1903854.
5. Jiao, L.; Li, J.K.; Richard, R.L.L.; Sun, Q.; Stracensky, T.; Liu, E.S.; Sougrati, M.T.; Zhao, Z.P.; Yang, F.; Zhong, S.C. Chemical vapour deposition of Fe-N-C oxygen reduction catalysts with full utilization of dense Fe-N_4 sites. *Nat. Mater*. **2021**, *20*, 1385-1391.
6. Balamurugan, J.; Nguyen, T.T.; Kim, N.H.; Kim, D.H.; Lee, J.H. Core-shell CuMo-oxynitride @N-doped graphene nanohybrids as multifunctional catalysts for rechargeable zinc-air batteries and water splitting. *Nano Energy*. **2021**, *85*, 105987.
7. Wu, M.J.; Wei, Q.L.; Zhang, G.X.; Qiao, J.L.; Wu, M.X.; Zhang, J.H.; Gong, Q.J.; Sun, S.H. Fe/Co double hydroxide/oxide nanoparticles on N-doped CNTs as highly efficient electrocatalysts for rechargeable liquid and quasi-solid-state zinc-air batteries. *Adv. Energy Mater*. **2018**, *8*, 1801836.
8. Irmawati, Y.; Balqis, F.; Destyorini, F.; Adios, C.G.; Yudianti, R.; Iskandar, F.; Sumboja, A. Cobalt nanoparticles encapsulated with N-doped bamboo-like carbon nanofibers as bifunctional catalysts for oxygen reduction/evolution reactions. *ACS Appl. Nano Mater*. **2023**, *6*, 2708-2718.
9. Yang, W.; Guo, B.; Guo, Z.; Wang, X.; Zeng, Y.; Guo, J.; Wu, M. Hollow porous carbon nanofibers with Fe-N-C modified by Fe_3O_4 nanoparticles for enhanced oxygen reduction reaction. *ACS Sustain. Chem. Eng.* **2023**, *11*, 8884-8892.
10. Wang, Q.; Kaushik, S.; Xiao, X.; Xu, Q. Sustainable zinc-air battery chemistry: Advances, challenges and prospects. *Chem. Soc. Rev.* **2023**, *52*, 6139-6190.
11. Xiao, X.; Zheng, Z.; Zhong, X.; Gao, R.; Piao, Z.; Jiao, M.; Zhou, G. Rational design of flexible Zn-based batteries for wearable electronic devices. *ACS Nano.* **2023**, *17*, 1764-1802.
12. Wang, L.; Xu, M.; Li, H.; Huang, Z.; Wang, L.; Isimjan, T.T.; Yang, X. Mn-doped Zn-MOF-derived porous N-doped carbon composites for oxygen reduction and flexible zinc-air batteries. *Inorg. Chem*. **2023**, *62*, 13284-13292.
13. Chang, J.; Zhang, Q.; Yu, J.; Jing, W.; Wang, S.; Yin, G.; Waterhouse, G.I.N.; Lu, S. Fe single-atom seed-mediated Fe_3C/Fe-N-C catalysts with outstanding bifunctional ORR/OER activity. *Adv. Sci.* **2023**, *10*, 2301656.
14. Fiorio, J.L.; Garcia, M.A.S.; Gothe, M.L.; Galvan, D.; Troise, P.C.; Conte-Junior, C.A.; Vidinha, P.; Camargo, P.H.C.; Rossi, L.M. Recent advances in the use of nitrogen-doped carbon materials for the design of noble metal catalysts. Coord. *Chem. Rev*. **2023**, *481*, 215053.
15. Jin, M.; Wang, R.; Jia, B.; Zhang, J.; Liu, H.; Lu, S.-Y. Achieving uniform Pt deposition site by tuning the surface microenvironment of bamboo-like carbon nanotubes. *Appl. Surf. Sci.* **2022**, *603*, 153201.
16. Fang, C.; Tang, X.; Yi, Q. Adding Fe/dicyandiamide to Co-MOF to greatly improve its ORR/OER bifunctional electrocatalytic activity. *Appl. Catal. B Environ.* **2024**, *341*, 123346.
17. Wang, M.; Chen, Z.; Song, Y.; Hu, Z.; Song, H.; Dong, S.; Yuan, D. Architecting N-doped Carbon Nanotube-Rich Carbon Nanofibers with Biomimetic Vine-Leaf-Whisker Structure as Robust Bifunctional Electrocatalysts for Rechargeable Zn-Air Batteries. *Inorg. Chem.* **2024**, *63*, 4373-4384
18. Kong, L.; Zhang, S.; Liu, Y.; Wu, H.; Fan, X.; Cao, Y.; Huang, J. Hierarchical architecture bioinspired CNTs/CNF electromagnetic wave absorbing materials. *Carbon.* **2023**, *207*, 198-206.
19. Wang, Z.; Ang, J.; Liu, J.; Ma, X.Y.D.; Kong, J.; Zhang, Y.; Yan, T.; Lu, X. FeNi alloys encapsulated in N-doped CNTs-tangled porous carbon fibers as highly efficient and durable bifunctional oxygen electrocatalyst for rechargeable zinc-air battery. *Appl. Catal. B.* **2020**, *263*, 118344.

 doi:10.20944/preprints202602.0665.v1

20. Zhao, X.; Abbas, S.C.; Huang, Y.; Lv, J.; Wu, M.; Wang, Y. Robust and Highly Active FeNi@NCNT Nanowire Arrays as Integrated Air Electrode for Flexible Solid-State Rechargeable Zn-Air Batteries. *Adv. Mater. Interfaces.* **2018**, *5*, 1701448.
21. Ding, W.; Saad, A.; Wu, Y.; Wang, Z.; Li, X. CNTs/CNF-supported multi-active components as highly efficient bifunctional oxygen electrocatalysts and their applications in zinc-air batteries. *Nano Res*. **2023**, *16*, 4793-4802.
22. Gao, C.; Mu, S.; Yan, R.; Chen, F.; Ma, T.; Cao, S. Recent Advances in ZIF-Derived Atomic Metal-N-C Electrocatalysts for Oxygen Reduction Reaction: Synthetic Strategies, Active Centers, and Stabilities. *Small.* **2022**, *18*, 2105409.
23. Dang, D.; Zhang, L.; Long, G.; Liu, C.; Fan, W.; Zheng, J.; Wang, T.; Liu, Q.; Han, X. Modulation the Coordination of Fe-Co Diatomic Sites with Boron Atom for Fuel Cells and Zn-Air Battery. *Appl. Catal. B Environ*. **2025**, *379*, 125679.
24. Li, M.; Lv, M.; Zheng, Y.; Zhu, M.; Feng, Q.; Guan, J.; Yu, X.; Shen, Y.; Hou, J.; Lu, Y.; Huang, N.; Ye, L. Bimetallic-Coordinated Covalent Triazine Framework-Derived FeNi Alloy Nanoparticle-Decorated Coral-Like Nanocarbons for Oxygen Electrocatalysis. ACS Appl. *Mater. Interfaces.* **2024**, *16*, 633-642.
25. Pan, Y.; Li, Y.; Nairan, A.; Khan, U.; Hu, Y.; Wu, B.; Sun, L.; Zeng, L.; Gao, J. Constructing FeNiPt@C Trifunctional Catalyst by High Spin-Induced Water Oxidation Activity for Zn-Air Battery and Anion Exchange Membrane Water Electrolyzer. *Adv. Sci*. **2024**, *11*, e2308205.
26. Chen, T.-H.; Ni, C.-S.; Lai, C.-Y.; Gull, S.; Chu, Y.-C.; Jao, W.-Y.; Hu, C.-C.; Liu, S.-F.; Chi, C.-C.; Chen, T.-Y.; Lee, J.-F.; Pao, C.-W.; Chen, J.-L.; Chen, H.-Y.; Huang, J.-H. Enhanced oxygen evolution and power density of Co/Zn@NC@MWCNTs for the application of zinc-air batteries. *J. Colloid Interface Sci.* **2025**, *679*, 119-131.
27. Dong, F.; Wu, M.; Chen, Z.; Chen, N.; Bakhtbidar, M.; Ruediger, A.; Zhang, G.; Sun, S. In situ reconstruction of bimetallic heterojunctions encapsulated in N/P co-doped carbon nanotubes for long-life rechargeable zinc-air batteries. *Nano Energy.* **2025**, *133*, 110497.
28. Yin, X.; Xi, W.; Wang, P.; Wu, T.; Liu, P.; Gao, B.; Zheng, Y.; Lin, B. In-situ construction of 2D β-$Co(OH)_2$ nanosheets hybridized with 1D N-doped carbon nanotubes as efficient bifunctional electrocatalyst for oxygen reduction and evolution reactions. *Chem. Eng. J*. **2025**, *503*, 158437.
29. Gu, T.; Shen, J.; Sun, Z.; Li, F.; Zhi, C.; Zhu, M.; Liu, J. Engineering Non-precious Trifunctional Cobalt-Based Electrocatalysts for Industrial Water Splitting and Ultra-High-Temperature Flexible Zinc-Air Battery. *Small.* **2024**, *20*, e2308355.
30. Hua, C.; Ye, D.; Chen, C.; Sun, C.; Fang, J.; Liu, L.; Bai, H.; Tang, Y.; Zhao, H.; Zhang, J. Engineering triple phase interface and axial coordination design of single-atom electrocatalysts for rechargeable Zn-air batteries. *Small.* **2025**, *21*, 2412696.
31. Wu, X.G.; Wang, R.; Ma, F.; Liu, X.L.; Jia, D.L.; Yang, H.C.; Liu, Y.P.; Wang, Z.X.; Zheng, H.Z.; Zhang, Y.N. FeCo-N encapsulated in nitrogen-doped carbon nanotubes as highly stable bifunctional electrocatalysts for zinc-air batteries. *Rare Met*. **2023**, *42*, 1526-1534.
32. Huang, C.; Zhang, Y.; Li, X.; Cao, H.; Guo, Y.; Zhang, C.Mn-incorporated Co_3O_4 bifunctional electrocatalysts for zinc-air batteries: An experimental and DFT study. *Appl. Catal. B Environ*. **2022**, *319*, 121909.
33. Zhang, X.; Yu, P.; Xing, G.; Xie, Y.; Zhang, X.; Zhang, G.; Sun, F.; Wang, L. Iron single atoms-assisted cobalt nitride nanoparticles to strengthen the cycle life of rechargeable Zn-air battery. *Small.* **2022**, *18*, 2205228, 10.1002/smll.202205228.

 doi:10.20944/preprints202602.0665.v1

34. Wang, Z.; Fan, C.; Chen, Y.; Yuan, Y.; Xue, J.; Yu, N.; Feng, J.; Yu, L.; Dong, L. NaCl-assisted electrospinning of bifunctional carbon fibers for high-performance flexible zinc-air batteries. *J. Colloid Interface Sci.* **2025**, *690*, 137325.
35. Ye, C.; Fan, P.; Wei, D.; Wang, J.; Xu, L. Nitrogen-doped carbon fibers loaded with $Co/Co_2Mn_3O_8$ alloy nanoparticles as bifunctional oxygen electrocatalysts for rechargeable zinc-air batteries. *J. Alloys Compd.* **2023**, *936*, 168210.